

A new regime of nanoscale thermal transport: Collective diffusion increases dissipation efficiency

Kathleen M. Hoogeboom-Pot^{a,b}, Jorge N. Hernandez-Charpak^{a,b}, Xiaokun Gu^c, Travis D. Frazer^{a,b}, Erik H. Anderson^d, Weilun Chao^d, Roger W. Falcone^d, Ronggui Yang^c, Margaret M. Murnane^{a,b}, Henry C. Kapteyn^{a,b,1}, and Damiano Nardi^{a,b}

^aJILA and Departments of ^bPhysics and ^cMechanical Engineering, University of Colorado, Boulder, CO 80309; and ^dLawrence Berkeley National Laboratory, Berkeley, CA 94720

This contribution is part of the special series of Inaugural Articles by members of the National Academy of Sciences elected in 2013.

Contributed by Henry C. Kapteyn, February 19, 2015 (sent for review February 3, 2015)

Understanding thermal transport from nanoscale heat sources is important for a fundamental description of energy flow in materials, as well as for many technological applications including thermal management in nanoelectronics and optoelectronics, thermoelectric devices, nanoenhanced photovoltaics, and nanoparticle-mediated thermal therapies. Thermal transport at the nanoscale is fundamentally different from that at the macroscale and is determined by the distribution of carrier mean free paths and energy dispersion in a material, the length scales of the heat sources, and the distance over which heat is transported. Past work has shown that Fourier's law for heat conduction dramatically overpredicts the rate of heat dissipation from heat sources with dimensions smaller than the mean free path of the dominant heat-carrying phonons. In this work, we uncover a new regime of nanoscale thermal transport that dominates when the separation between nanoscale heat sources is small compared with the dominant phonon mean free paths. Surprisingly, the interaction of phonons originating from neighboring heat sources enables more efficient diffusive-like heat dissipation, even from nanoscale heat sources much smaller than the dominant phonon mean free paths. This finding suggests that thermal management in nanoscale systems including integrated circuits might not be as challenging as previously projected. Finally, we demonstrate a unique capability to extract differential conductivity as a function of phonon mean free path in materials, allowing the first (to our knowledge) experimental validation of predictions from the recently developed first-principles calculations.

nanoscale thermal transport | nondiffusive transport | mean free path spectroscopy | high harmonic generation | ultrafast X-rays

Critical applications including thermoelectrics for energy harvesting, nanoparticle-mediated thermal therapy, nanoenhanced photovoltaics, and thermal management in integrated circuits require a comprehensive understanding of energy flow at the nanoscale. Recent work has shown that the rate of heat dissipation from a heat source is reduced significantly below that predicted by Fourier's law for diffusive heat transfer when the characteristic dimension of the heat source is smaller than the mean free path (MFP) of the dominant heat carriers (phonons in dielectric and semiconductor materials) (1–6). However, a complete fundamental description of nanoscale thermal transport is still elusive, and current theoretical efforts are limited by a lack of experimental validation.

Diffusive heat transfer requires many collisions among heat carriers to establish a local thermal equilibrium and a continuous temperature gradient along which energy dissipates. However, when the dimension of a heat source is smaller than the phonon MFP, the diffusion equation is intrinsically invalid because phonons move ballistically without collisions. The rate of nanoscale heat dissipation is significantly lower than the diffusive prediction such that smaller heat sources appear increasingly inefficient in dissipating heat. Furthermore, heat-carrying phonons in real

materials have a wide distribution of MFPs, from several nanometers to hundreds of microns (7). For a given nanoscale heat source size, phonons with MFPs shorter than the hot-spot dimension remain fully diffusive and contribute to efficient heat dissipation and a high thermal conductivity (or equivalently, a low thermal resistivity). In contrast, phonons with long MFPs travel ballistically far from the heat source before scattering, with an effective thermal resistivity far larger than the diffusive prediction. Phonons with intermediate MFPs fall in between; here, heat transfer is quasiballistic with varying degrees of reduced contributions to the conduction of heat away from the nanoscale source. Most work to date explored the reduction in heat transfer from functionally isolated microscale and nanoscale heat sources (1–5). Indeed, characterizing heat transfer from micro/nanostructures with varying size can be used to experimentally measure cumulative phonon MFP spectra of materials (2, 8, 9), with the proof-of-principle demonstrated for long-MFP (>1- μ m) phonons in silicon (3).

In this work, we show through both experiment and theory that the size of the heat source is not the only important scale that determines nanoscale heat dissipation. We identify a new regime of thermal transport that occurs when the separation between nanoscale heat sources is smaller than the average phonon MFP. Surprisingly, we find that when phonons from neighboring heat sources interact, more of them dissipate heat in a diffusive

Significance

A complete description of nanoscale thermal transport is a fundamental problem that has defied understanding for many decades. Here, we uncover a surprising new regime of nanoscale thermal transport where, counterintuitively, nanoscale heat sources cool more quickly when placed close together than when they are widely separated. This increased cooling efficiency is possible when the separation between nanoscale heat sources is comparable to the average mean free paths of the dominant heat-carrying phonons. This finding suggests new approaches for addressing the significant challenge of thermal management in nanosystems, with design implications for integrated circuits, thermoelectric devices, nanoparticle-mediated thermal therapies, and nanoenhanced photovoltaics for improving clean-energy technologies.

Author contributions: K.M.H.-P., J.N.H.-C., E.H.A., W.C., R.W.F., R.Y., M.M.M., H.C.K., and D.N. designed research; K.M.H.-P., J.N.H.-C., T.D.F., and D.N. performed research; K.M.H.-P., J.N.H.-C., X.G., R.Y., and D.N. contributed new reagents/analytic tools; E.H.A. and W.C. fabricated samples; K.M.H.-P., J.N.H.-C., T.D.F., and D.N. analyzed data; and K.M.H.-P., J.N.H.-C., X.G., T.D.F., R.Y., M.M.M., H.C.K., and D.N. wrote the paper.

The authors declare no conflict of interest.

Freely available online through the PNAS open access option.

¹To whom correspondence should be addressed. Email: henry.kapteyn@colorado.edu.

This article contains supporting information online at www.pnas.org/lookup/suppl/doi:10.1073/pnas.1503449112/-DCSupplemental.

regime, thus counteracting the inefficiency caused by ballistic effects in the case of isolated heat sources. This collective behavior can increase heat transfer to near the diffusive limit. Most importantly, the appearance of this “collectively diffusive” regime mitigates the scaling problems for thermal management in nanoelectronics, which may not be as serious as projected (2, 10, 11). Finally, we use this previously unobserved phenomenon to extract the contribution to thermal transport from specific regions of the phonon MFP spectrum, opening up a new approach for thermal transport metrology and MFP spectroscopy. This is because by varying both nanostructure size and separation, an effective phonon filter is introduced that suppresses specific sections of MFP contributions to thermal conductivity. We compare our extracted phonon MFP spectra with predictions from first-principles calculations and find excellent agreement between experiment and theory. Looking forward, we have a unique capability for characterizing phonon transport in novel materials where predictions do not yet exist.

Fig. 1 illustrates the differences between the three regimes of heat transport from nanoscale heat sources—purely diffusive, quasiballistic, and collectively diffusive. Quasiballistic transport (Fig. 1B) dominates when the size of isolated nanoscale heat sources is smaller than dominant phonon MFPs. In the new collectively diffusive regime we uncovered (Fig. 1C), the separation between heat sources is small enough that long-MFP phonons, whose contribution to heat dissipation would normally be limited by the small size of nano-heat sources, can once again play a significant role and restore heat transfer efficiency to near the diffusive limit. Although these phonons travel ballistically away from each individual heat source, they can scatter with

phonons originating from a neighboring heat source, thus creating an effectively larger heat source size. In the limiting case, the spacing between heat sources vanishes and this regime approaches heat dissipation from a uniformly heated layer.

Experiment

In our experiment, arrays of nickel nanowires were fabricated by e-beam lithography and lift-off techniques to form periodic gratings on the surface of sapphire and silicon substrates. The nanowire line widths L range from 750 nm down to 30 nm, with period $P = 4L$ and a rectangular profile height of ~ 13.5 nm. The use of nano-patterned structures rather than optical absorption allows us to explore the dynamics of heat sources much smaller than the diffraction limit of visible light. The metallic nanowires are heated by a 25-fs pump pulse centered at a wavelength of 800 nm. The sapphire substrate is transparent at this wavelength, whereas the silicon substrate has such a long absorption depth that any small, uniform heating of the substrate can be neglected. Laser excitation thus creates an array of nanoscale hot spots (lines) on the surface of a cold substrate. Because all nanostructures are fabricated on the same substrate at the same time, the intrinsic thermal boundary resistivity at the interface between the metallic line and the substrate will be constant across all samples: any variation in efficiency of heat dissipation as the hot-spot size or spacing is varied can thus be attributed to different regimes of thermal transport.

The laser-induced thermal expansion and subsequent cooling of the nanogratings is probed using coherent extreme UV (EUV) light centered at a wavelength of 29 nm, created by high harmonic up-conversion of an 800-nm Ti:sapphire laser (12). The time delay between the EUV probe pulse and the laser pump pulse is adjusted using a mechanical delay stage between -400 and $+8,000$ ps, with step size as small as 1 ps. As the EUV light diffracts from the periodic array of Ni nanowires, expansion and cooling of the nanogratings changes the diffraction efficiency, and this signal is recorded by a CCD camera as a function of delay time between pump and probe pulses. Examples of this dynamic signal are shown in Fig. 24. [Note that more details of the experimental setup are described elsewhere (13, 14) and in *SI Text, section S1*.] Because the reflectivities of these materials do not change with temperature at EUV wavelengths (15), the change in the diffraction signal can be uniquely attributed to physical deformations in the surface profile. Moreover, because the thermally expanded nanowires will change the diffraction signal as long as their temperature is higher than their initial state, this serves as a measure of the cooling rate of the nanowires rather than the rate of heat transfer across a specific distance as in optical transient grating (6) or buried-layer heating experiments (16). Thus, the data of Fig. 24 can be used to directly extract the average thermal expansion and relaxation of each individual nanowire induced by laser heating and subsequent heat dissipation into the substrate, in addition to the surface deformations caused by acoustic waves launched by the initial impulsive expansion (13, 14, 17).

Theory

To understand the different regimes of thermal transport illustrated in Fig. 1, we consider three models: (i) the model described in our previous work that assumes isolated heat sources (1); (ii) an analytical model we develop here to account for interactions of phonons originating from neighboring heat sources using a gray, single-phonon-MFP approximation; and (iii) a more advanced interacting model that includes a distribution of phonon MFPs. As discussed in detail below, this interacting multi-MFP model allows us to extract MFP-dependent contributions to thermal conductivity for MFPs as short as 14 nm for the first time (to our knowledge), providing data that can be directly compared with predictions from first-principles density functional theory (DFT).

To quantify the deviations from diffusive heat transport, we first build upon methods similar to those described by Siemens

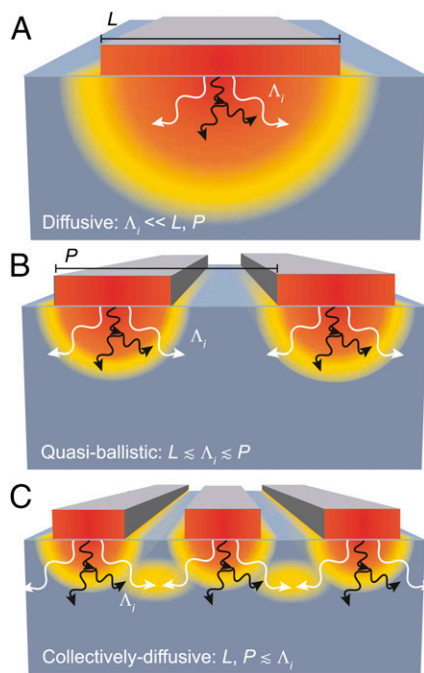


Fig. 1. Nanoscale heat transport is determined by the interplay between three length scales: the size of the heat sources L , the spacing of the heat sources P , and the MFPs λ_i of heat-carrying phonons. Materials support a broad distribution of MFPs, represented here by short (black)- and long (white)-MFP phonons. (A) When all MFPs are smaller than L , heat dissipation is fully diffusive. (B) As L shrinks, long-MFP phonons travel ballistically, decreasing the rate of heat dissipation relative to diffusive predictions. Short-MFP phonons remain diffusive. (C) When both L and P shrink, long-MFP phonons originating from neighboring heat sources interact as they would if they originated from a single, large heat source, enabling more efficient diffusive-like heat transfer.

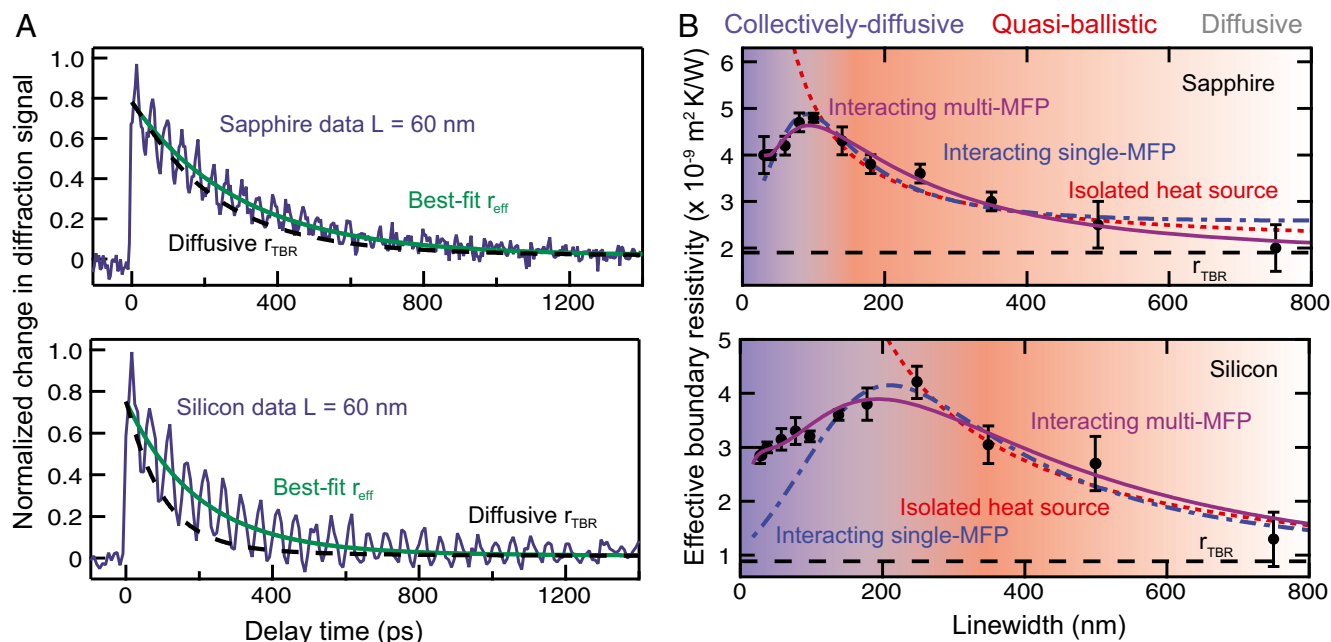


Fig. 2. Effective thermal boundary resistivities are extracted from dynamic EUV diffraction. (A) Dynamic diffraction from 60-nm-wide nickel lines on sapphire (Top) and silicon (Bottom) display a sudden rise due to impulsive thermal expansion following laser heating, a long decay due to thermal relaxation, and oscillations due to surface acoustic waves. Dashed black lines plot the diffusive prediction, which significantly underestimates the thermal decay time. Green lines plot the decay using a best fit to the effective thermal boundary resistivity. (B) Extracted effective resistivities for each line width L on both substrates increase with decreasing line width until the periods (equal to $4L$) are comparable to the average phonon MFP. For smaller periods (spacing), the effective resistivity decreases and approaches the diffusive limit (black dashed line). The error bars represent the SD among multiple datasets for the same line width samples. Dotted red lines: predictions for isolated heat sources based on the gray model. Dash-dot blue lines: gray model including the onset of the collectively diffusive regime. Solid purple lines: more complete model that includes contributions from multiple phonon MFPs.

et al. (1), but including more comprehensive finite-element physical modeling (18) to improve data reduction accuracy. We model our system using diffusive heat conduction theory, while allowing the effective thermal boundary resistivity (which sets the temperature discontinuity across the boundary between the nickel nanowires and the substrate) to vary as a function of line width to account for nondiffusive effects in the substrate near the heat source.

We use accurate sample dimensions (height, line width, and period) characterized by atomic force microscopy (*SI Text, section S1*). Fresnel optical propagation is then used to calculate the diffraction signal from the simulated surface deformations. The effective boundary resistivity, r_{eff} , that provides the best fit to the experimental data of Fig. 2A represents the sum of two terms: first, the constant intrinsic thermal boundary resistivity, r_{TBR} , that originates from the material difference between nickel and substrate; and second, a correction term, r_{Corr} , due to nondiffusive transport in the substrate close to the heat source when either L or P is smaller than MFPs. Although this is a similar effective correction for nondiffusive transport near isolated nanoscale heat sources as that used in previous works (2–6), by assigning the nondiffusive contribution to the thermal boundary resistivity rather than to changes in the thermal conductivity of the substrate, we maintain a simple modeling geometry and avoid the need to assume a particular region of the substrate in which an effective conductivity change should apply. Further discussion can be found in *SI Text, section S2*.

The effective resistivity results are plotted in Fig. 2B. For large line widths on both sapphire and silicon substrates, the effective resistivity converges toward a constant value—the intrinsic thermal boundary resistivity. As the line width approaches the dominant phonon MFPs in the substrate, the effective resistivity rises as thermal transport becomes quasiballistic and the contribution to heat dissipation of long-MFP phonon modes is suppressed (1, 3, 8). This behavior was successfully described in past work using a simple gray model for sapphire and fused silica, which assumes

a single-phonon MFP to loosely describe a weighted average of the MFPs from all of the phonon modes contributing to thermal transport in a given material. According to this model, a ballistic correction term proportional to $\Lambda_{\text{gray}}/(L/2)$ can be added to the intrinsic thermal boundary resistivity (1, 19); this prediction is plotted in dotted red in Fig. 2B.

However, as the line width (and period) shrinks further, Fig. 2B shows that the effective resistivity starts to decrease rather than continuing to increase. The constant grating duty cycle for our series of samples means that the smallest-line width nanowires are also those with the smallest separation between neighboring heat sources. Thus, for small line widths, the separation becomes comparable to dominant phonon MFPs. For silicon, this peak in r_{eff} is shifted toward longer line widths/periods compared with sapphire because the phonon MFP distribution in silicon is also shifted toward longer MFPs, i.e., silicon has a longer average MFP than sapphire (1, 6). As illustrated in Fig. 1C, in this collectively diffusive regime, longer-MFP phonons from neighboring heat sources interact with each other as they would if they originated from a single, large heat source, leading to diffusive-like heat dissipation and decreasing the effective resistivity. The quasiballistic model for isolated heat sources clearly fails to capture this experimental observation, and a new model for r_{Corr} is required to account for the transition to this previously unobserved and unobserved collectively diffusive regime.

We propose to use the concept of a notch filter in the MFP spectrum to describe the effects of grating line width and separation, shown schematically in Fig. 3A. The notch filter suppresses the contribution of phonon modes with MFPs that fall between the line width L and period P of the nanogratings. Thus, if the grating period (separation) remains large while the line width is decreased, one would expect the effective boundary resistivity to continue to rise, as shown in the red dotted lines of Fig. 2B. This is because the contributions of all phonon modes

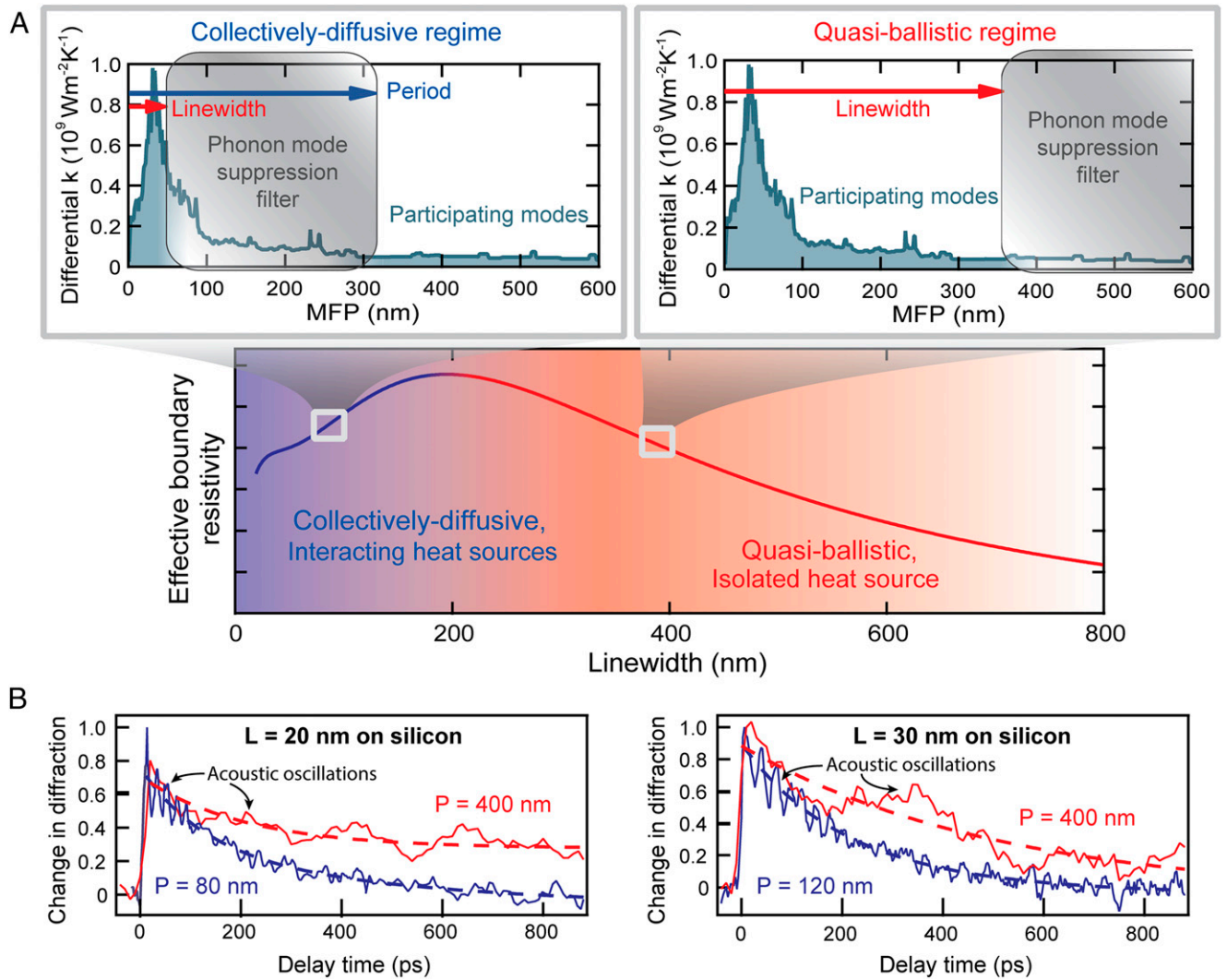


Fig. 3. Line width and period define a suppression filter for phonon MFP spectra. (A) The observed increase in effective thermal boundary resistivity for small line widths L is due to the suppression of the contribution to thermal conductivity of phonon modes with MFP larger than L . Decreasing the period P can reactivate modes with MFP larger than P , decreasing the effective resistivity. In the limiting case of a uniformly heated layer, P approaches L and all phonon modes participate in thermal transport. We use as an example the smoothed differential conductivity distribution for silicon (top graphs, green line), calculated from first-principles DFT (SI Text, section S4). (B) A comparison of the thermal decay of small line width gratings for two different periods directly validates the prediction of the suppression filter model, i.e., small line widths spaced far apart (red lines) exhibit a slower initial thermal decay than small line widths spaced closer together (blue lines). The dashed lines provide a guide to the eye for the thermal decay through the center of the acoustic oscillations.

with MFPs longer than the line width L are suppressed in the quasiballistic regime of isolated heat sources. On the other hand, if the grating period shrinks, long-MFP phonon modes start to contribute again because phonons originating from neighboring heat sources interact with each other as they would in a bulk system, so the effective boundary resistivity should recover toward the bulk value, as seen experimentally in Fig. 2B. If this picture is true, then a nanograting with a small line width and large period (i.e., wide filter) should exhibit a slower thermal decay than the same line width grating with shorter period (i.e., narrower filter). Using a set of periodic nickel nanowires on silicon with varied duty cycle, we directly observed this pronounced difference as shown in Fig. 3B.

To build an analytical expression for r_{Corr} based on this idea, we use the concept of a phonon conductivity suppression function, $S(L, P, \Lambda)$, similar to those described by others (8, 20). This suppression function is applied to a bulk differential conductivity

spectrum versus phonon MFP of the substrate, $k(\Lambda_i)$, to calculate an effective nanoscale conductivity K_{nano} :

$$K_{\text{nano}} = \sum_i k(\Lambda_i) \cdot S(L, P, \Lambda_i). \quad [1]$$

We then relate r_{Corr} to the change in conductivity represented by this suppression:

$$r_{\text{Corr}} = A \left(\frac{1}{K_{\text{nano}}} - \frac{1}{K_{\text{bulk}}} \right), \quad [2]$$

where A collects geometrical constants (discussed further in SI Text, section S3) and K_{bulk} is the bulk conductivity of the substrate, simply given by $\sum_i k(\Lambda_i)$. For a given phonon MFP Λ_i , S must approach unity in the diffusive regime when both L and P are large and at the limit of uniform heating when $L = P$. For the limit of small, isolated heat sources when $L \rightarrow 0$ but P is large, $S \rightarrow L / (2\Lambda)$ to reproduce the behavior of the previously published

quasiballistic model (1, 21). Finally, the effects of L and P should be the same but opposite to each other so that L suppresses phonon mode contributions in the same way as P reactivates them. To capture these behaviors along with smooth transitions among regimes, the two effects are represented by a special case of the generic family of logistic functions, where the total suppression function is written as follows:

$$S = \tanh\left(\frac{L}{2\Lambda}\right) + \left[1 - \tanh\left(\frac{P}{2\Lambda}\right)\right]. \quad [3]$$

More details of this suppression function can be found in *SI Text, section S3*. Although more rigorous methods of deriving suppression functions for various experimental geometries are currently being explored (9, 20, 22), none has yet sought to account for closely spaced heat sources or an accompanying reintroduction of phonon modes. Eq. 3 represents the first attempt (to our knowledge) to include the contribution of heat source spacing and offers a model that is simple enough for fast integration into existing models of heat transfer in nanoscale devices, for example, but complex enough to capture the previously unobserved behavior and make successful predictions.

To test this new model for r_{Corr} , we first assume the simple single-MFP (gray) model (where the MFP distribution is a delta function). The resulting predictions are shown in the blue curves in Fig. 2B. Specifically, r_{Corr} in this case is given by the following:

$$r_{\text{Corr, gray}}(L, P) = \frac{A}{K_{\text{bulk}}} \left(\frac{1}{S(L, P, \Lambda_{\text{gray}})} - 1 \right). \quad [4]$$

Fitting this interacting model to the r_{eff} data for sapphire, we extract values for r_{TBR} and Λ_{gray} that are consistent with previous results (1): $\Lambda_{\text{gray, int}} = 131 \pm 11$ nm, $r_{\text{TBR, int}} = 2.58 \pm 0.19 \times 10^{-9}$ m²-K/W. This good agreement with the previous larger-line width data and the accurate fit for the full range of our data validate our interacting r_{Corr} model as an improved method to account for nanoscale size effects in heat transport—for both quasiballistic and collectively diffusive regimes. Interestingly, this single-MFP model provides a reasonable approximation for the entire range of heat transport in sapphire.

For silicon, the interacting r_{Corr} follows the general shape of the data and yields $\Lambda_{\text{gray, int}} = 306 \pm 17$ nm, which is consistent with previously reported values (6). However, the interacting gray-model approach, although more successful than the isolated model, fails to capture the additional structured tail in effective resistivity that appears for very small line widths and periods, below $L = 100$ nm. The failure of this approach is not surprising, because the single-MFP model is known to be a poor approximation for silicon with its broad distribution of phonon MFPs (8, 20).

Discussion of Collectively Diffusive Regime and Extension to Phonon Mode Conductivity Spectra

Having developed and validated the new model to capture the transitions from diffusive, to quasiballistic, to collectively diffusive regimes, we can now extend our calculations beyond the simple single-MFP model and use our data to extract the MFP-dependent contributions to thermal conductivity in different materials down to MFPs as small as 14 nm for the first time (to our knowledge). Because line width and period set the location and width of the effective notch filter in the phonon MFP spectrum, each configuration uniquely samples the contribution to thermal conductivity of different MFP ranges of phonon modes with a resolution controlled primarily by the number of configurations tested. The larger the resistivity correction needed for a given nanograting, the stronger the conductivity contribution of phonon modes that were suppressed.

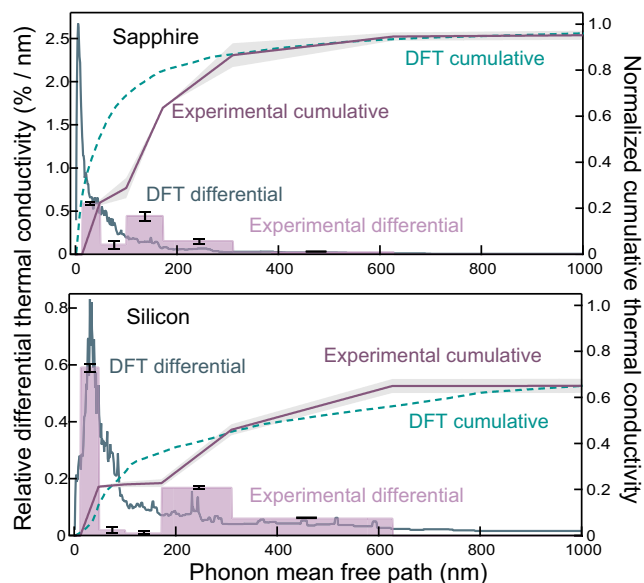


Fig. 4. By fitting r_{eff} with multiple bins of phonon modes, the weights $k(\Lambda_i)$ assigned to those bins give the average relative contribution to the differential thermal conductivity (purple shading). Both differential (distributions) and cumulative (lines) conductivities are normalized to the total bulk conductivity. For sapphire (Top), our data (solid purple line) and first-principles DFT calculations (dashed green line) indicate there are no significant contributions from long-MFP phonons, so the cumulative curves approach unity at 1 μm . For silicon (Bottom), our data are consistent with large contributions from longer MFPs.

To extract information about the differential conductivity spectrum, we use the full multi-MFP form of r_{Corr} , given by the following:

$$r_{\text{Corr}}(L, P) = A \left(\frac{1}{\sum_i k(\Lambda_i) S(L, P, \Lambda_i)} - \frac{1}{K_{\text{bulk}}} \right). \quad [5]$$

We partition the full sum in bins according to the MFP sensitivity of each grating configuration (*SI Text, section S3*). Then by fitting our set of r_{eff} data as $r_{\text{eff}} = r_{\text{TBR}} + r_{\text{Corr}}$, we extract the average $k(\Lambda_i)$ that is associated with all modes Λ_i within each bin, thus assessing the relative contributions to thermal conductivity of each region of the phonon MFP spectrum (plotted in Fig. 4). By limiting the number of bins to be no more than one-half of our number of data points, we ensure a conservative, well-conditioned fit, although we note that changing the bin number does not substantially alter the trends we observe. As shown by the purple curves in Fig. 2B, for sapphire, this procedure matches the experimentally measured r_{eff} as well as the gray model for interacting heat sources. For silicon, this more complete multiple-MFP interacting model is able to match our experimental measurements of thermal boundary resistivity over diffusive, quasiballistic and collectively diffusive regimes, including the exceptionally slow drop in resistivity for small line widths below 100 nm.

Although the number of experimental data points limits the number of regions we can reasonably consider in this first demonstration, this approach still offers unprecedented experimental access to the differential thermal conductivity contributions of phonons with different MFPs and for benchmarking theoretical predictions, including those from first-principles DFT calculations shown in Figs. 3A and 4. In particular, our experimental data across all MFP ranges measured in silicon are in very good agreement with our DFT calculations [which also agree with those in the literature (8)]. However, some small discrepancies appear for

phonon MFPs around ~ 100 nm, where experimental verification was not possible before. Differences between the experimental and theoretical spectra in this region may also be exaggerated by our limited set of small-line width gratings; increased resolution with a larger sample set can address this issue. Our data are also consistent with observations by others that emphasize significant contributions from long-MFP ($>1\text{-}\mu\text{m}$) modes (2, 3, 6), but the limited number of data points we have for structures much larger than the average phonon MFP results in a relatively large uncertainty in this region. For the purpose of comparison in Fig. 4, we normalized the experimental spectra in silicon by assuming the integrated conductivity up to $1\text{ }\mu\text{m}$ should match that calculated by DFT.

For sapphire, both calculation and experimental data imply that phonons with MFPs shorter than $1\text{ }\mu\text{m}$ are responsible for $>95\%$ of the thermal conductivity. The discrepancy below 300 nm between experimental and theoretical curves (apparent in the cumulative distribution) is due to two factors. First, the sharper rise in the DFT cumulative curve arises due to the very strong short-MFP peak in the conductivity spectrum—a peak that lies at $\sim 5\text{ nm}$, below the lower bound of our experimental sensitivity (14 nm) using 30-nm structures. Thus, the experimental data simply do not include the shortest phonon MFP peak. Second, because of the complex crystal structure of sapphire, the DFT calculations required the use of relatively small interaction-distance cutoffs for determining the harmonic and anharmonic force constants, which may cause a larger error in the predictions than for silicon.

There are two significant advantages of our EUV-based technique compared with previously reported MFP spectroscopy techniques. First, our approach that combines nanoheaters with the phase sensitivity of short-wavelength probes is the only way to experimentally access dimensions far below 100 nm to directly resolve the contributions of phonons with MFP down to 14 nm . Other approaches require numerical extrapolation techniques and interpretation, which are still being developed (9). Second, characterizing phonon MFP spectra by harnessing interacting nanoscale heat sources allows us to probe arbitrary segments of the MFP spectrum for any novel material, enabling direct access to the differential, rather than only the cumulative, MFP distribution.

The ability to experimentally extract a phonon MFP distribution down to such small MFPs offers an exceptional, useful

method for validating existing first-principles predictions across the whole range of phonon MFPs significant for heat conduction, as well as the first access to such information for more complex materials where calculations have not yet been performed. Furthermore, combined knowledge of both the differential and cumulative spectra may offer intriguing insight into the full MFP spectrum with the detail necessary for accurate prediction of heat transfer in nanostructured systems.

Conclusion

In summary, we uncover a new regime of nanoscale thermal transport that dominates when the separation between nanoscale heat sources is small compared with the dominant phonon MFPs. We also present a new approach for characterizing the relative contributions of phonons with different MFPs that participate strongly in heat conduction. In particular, we can probe the small-MFP region, which has been previously inaccessible to experiment. This unique capability is important as the need for precise phonon MFP distributions in complex nanostructures becomes more pressing—for both fundamental understanding and to harness systems where modeling does not yet exist. In the future, because bright soft X-ray high harmonic sources can now reach wavelengths below 1 nm (23), this approach can be extended even further into the deep nanoregime. In addition, more comprehensive and fundamental insight into nanoscale thermal transport may be possible by adopting the framework created to bridge all types of anomalous diffusion (24–27), which does not rely on effective diffusion models for inherently nondiffusive heat transfer. Finally, the efficient, collectively diffusive regime of thermal transport that we observe for the first time can potentially mitigate projected problems for thermal management in nanoelectronics, where the power density is likely to increase as the individual nanostructures shrink in size (10, 11). It also highlights important design implications for nanostructured materials and devices for energy and biomedical applications.

ACKNOWLEDGMENTS. We gratefully acknowledge support from the US Department of Energy Basic Energy Sciences and the Semiconductor Research Corporation, and used facilities provided by the National Science Foundation (NSF) Engineering Research Center for EUV Science and Technology and a National Security Science and Engineering Faculty Fellowship award. K.M.H.-P. acknowledges support from the NSF under Award DGE 1144083. X.G. and R.Y. acknowledge the NSF CAREER award and Air Force Office of Scientific Research support.

- Siemens ME, et al. (2010) Quasi-ballistic thermal transport from nanoscale interfaces observed using ultrafast coherent soft X-ray beams. *Nat Mater* 9(1):26–30.
- Regner KT, et al. (2013) Broadband phonon mean free path contributions to thermal conductivity measured using frequency domain thermoreflectance. *Nat Commun* 4:1640.
- Minnich AJ, et al. (2011) Thermal conductivity spectroscopy technique to measure phonon mean free paths. *Phys Rev Lett* 107(9):095901.
- Koh YK, Cahill DG (2007) Frequency dependence of the thermal conductivity of semiconductor alloys. *Phys Rev B* 76(7):075207.
- Freedman JP, et al. (2013) Universal phonon mean free path spectra in crystalline semiconductors at high temperature. *Sci Rep* 3:2963.
- Johnson JA, et al. (2013) Direct measurement of room-temperature nondiffusive thermal transport over micron distances in a silicon membrane. *Phys Rev Lett* 110(2):025901.
- Esfarjani K, Chen G, Stokes HT (2011) Heat transport in silicon from first-principles calculations. *Phys Rev B* 84(8):085204.
- Yang F, Dames C (2013) Mean free path spectra as a tool to understand thermal conductivity in bulk and nanostructures. *Phys Rev B* 87(3):035437.
- Minnich AJ (2012) Determining phonon mean free paths from observations of quasiballistic thermal transport. *Phys Rev Lett* 109(20):205901.
- King SW, Simka H, Herr D, Akinaga H, Garner M (2013) Research updates: The three M's (materials, metrology, and modeling) together pave the path to future nanoelectronic technologies. *Appl Phys Lett Mater* 1:040701.
- Pop E, Sinha S, Goodson KE (2006) Heat generation and transport in nanometer-scale transistors. *Proc IEEE* 94(8):1587–1601.
- Rundquist A, et al. (1998) Phase-matched generation of coherent soft X-rays. *Science* 280(5368):1412–1415.
- Nardi D, et al. (2013) Probing limits of acoustic nanometrology using coherent extreme ultraviolet light. *Proc SPIE* 8681:86810N-1–86810N-8.
- Li Q, et al. (2012) Generation and control of ultrashort-wavelength two-dimensional surface acoustic waves at nanoscale interfaces. *Phys Rev B* 85(19):195431.
- Tobey RI, et al. (2007) Ultrafast extreme ultraviolet holography: Dynamic monitoring of surface deformation. *Opt Lett* 32(3):286–288.
- Highland M, et al. (2007) Ballistic-phonon heat conduction at the nanoscale as revealed by time-resolved x-ray diffraction and time-domain thermoreflectance. *Phys Rev B* 76(7):075337.
- Nardi D, et al. (2011) Probing thermomechanics at the nanoscale: Impulsively excited pseudosurface acoustic waves in hypersonic phononic crystals. *Nano Lett* 11(10):4126–4133.
- COMSOL, Inc. (2013) COMSOL Multiphysics, Version 4.3b (COMSOL, Inc., Burlington, MA).
- Chen G, Borca-Tasciuc D, Yang RG (2004) Nanoscale heat transfer. *Encyclopedia of Nanoscience and Nanotechnology*, ed Nalwa HS (American Scientific Publishers, Valencia, CA), Vol 7, pp 429–459.
- Maznev AA, Johnson JA, Nelson KA (2011) Onset of nondiffusive phonon transport in transient thermal grating decay. *Phys Rev B* 84(19):195206.
- Chen G (1996) Nonlocal and nonequilibrium heat conduction in the vicinity of nanoparticles. *J Heat Transfer* 118:539–545.
- Regner KT, McGaughey AJH, Malen JA (2014) Analytical interpretation of nondiffusive phonon transport in thermoreflectance thermal conductivity measurements. *Phys Rev B* 90(6):064302.
- Popmintchev T, et al. (2012) Bright coherent ultrahigh harmonics in the keV x-ray regime from mid-infrared femtosecond lasers. *Science* 336(6086):1287–1291.
- Metzler R, Klafter J (2000) The random walk's guide to anomalous diffusion: A fractional dynamics approach. *Phys Rep* 339(1):1–77.
- Liu S, Xu XF, Xie RG, Zhang G, Li BW (2012) Anomalous heat conduction and anomalous diffusion in low dimensional nanoscale systems. *Eur Phys J B* 85(1):1–20.
- Liu S, Hånggi P, Li N, Ren J, Li B (2014) Anomalous heat diffusion. *Phys Rev Lett* 112(4):040601.
- Vermeersch B, et al. (2014) Thermal interfacial transport in the presence of ballistic heat modes. *Phys Rev B* 90(1):014306.

Supporting Information

Hoogeboom-Pot et al. 10.1073/pnas.1503449112

SI Text

S1. Experimental Setup and Samples

For the time-resolved diffraction measurement, we used the pump–probe system described in our previous work (1, 2). The pump and probe pulses are derived from the same Ti:sapphire amplifier system (centered at a wavelength of 800 nm, with 4- to 6-kHz repetition rate, 1.5- to 2-mJ pulse energy, and 25-fs pulse length) as shown in Fig. S1. The probe beam is focused into an argon-filled hollow waveguide to generate short-wavelength (centered at 29 nm) extreme UV (EUV) light via the nonlinear process of high-order harmonic generation (3). The very short wavelength and interferometric diffraction measurement gives us high lateral and axial spatial resolution to follow the dynamics in nanostructured systems with sensitivity to surface displacements at the picometer scale. The EUV beam is focused onto the sample using a grazing-incidence toroidal mirror to a diameter of $\sim 100\ \mu\text{m}$ (smaller than the $120 \times 120\text{-}\mu\text{m}$ patterned area).

To ensure uniform heating of the nanogratings, the pump beam is kept relatively large with a diameter of $\sim 400\text{--}500\ \mu\text{m}$ and a fluence of $\leq 10\ \text{mJ}/\text{cm}^2$. The height of the nickel nanostructures is chosen to be less than or equal to the absorption depth of the infrared pump light for nearly uniform heating in the vertical direction as well. By testing the thermal decay dynamics with multiple pump fluences, we ensure that all our measurements are taken within the linear regime of heat transfer.

Because nickel is a metal, most of the heat is carried by electrons inside the nanostructures. Strong electron–phonon coupling ensures that the lattice has thermalized with the electrons within the first 10 ps—much faster than the timescale of thermal decay we are investigating. Because electron mean free paths (MFPs) are much smaller than all of the structures we explore, no significant nanoscale thermal conductivity effects should be expected in the nickel nanostructures.

To accurately characterize the sample (in terms of line width, height, and period of the nanograting) and design the unit cell in the finite-element simulations of the heat transport and thermal expansion, we imaged each sample using atomic force microscopy and scanning electron microscopy. We observed good uniformity across the nanostructures, as shown in the representative images in Fig. S2 B and C.

S2. Finite-Element Multiphysics Modeling for Experimental Data Analysis

To quantitatively analyze the different regimes of nanoscale thermal transport illustrated in Fig. 1 of the main text, we use a similar approach as that described by Siemens et al. (4), but with a more comprehensive finite-element physical modeling approach (5) to reduce uncertainty in the comparison between experimental observations and the simulation output. We model our experimental observation using a 2D simulation unit cell with the plane strain approximation to follow the full thermal expansion and cooling dynamics of the nickel nanogratings on the sapphire and silicon substrates (6). The nanograting geometry allows for periodic boundary conditions for the temperature T and the displacement \mathbf{u} on the sides of the unit cell. All mesh points are initialized at room temperature and zero displacement ($T = 293\ \text{K}$, $\mathbf{u} = 0$). The top boundaries are free to move but heat flux across them is set to zero (no radiative heat dissipation). Continuity in the displacement is enforced at the interface between the Ni structure and the substrate, effectively joining the two materials such that no slipping is allowed. The bottom

boundary is fixed, and the heat flux across it is also set to zero. The height of the substrate section is set to $10\ \mu\text{m}$, much larger than the maximum thermal penetration depths of $0.85\ \mu\text{m}$ in silicon and $0.35\ \mu\text{m}$ in sapphire, to ensure no excess heat reaches the bottom boundary during the simulation time (up to 8 ns). An example of the top region of the unit cell geometry and mesh profile for the finite-element simulations is illustrated in Fig. S3.

Unlike Siemens et al. (4), we incorporate the inertial terms in the initial thermal expansion and solve the coupled equations for the profiles of T and \mathbf{u} in the time domain (7):

$$\nabla \cdot (\mathbf{c} : \nabla(\mathbf{u} - \alpha \Delta T)) = \rho \frac{\partial^2 \mathbf{u}}{\partial t^2}, \quad [\text{S1}]$$

$$\rho C_p \frac{\partial T}{\partial t} + \rho C_p \mathbf{u} \cdot \nabla T = \nabla \cdot (K_{\text{bulk}} \nabla T) + Q, \quad [\text{S2}]$$

where \mathbf{c} is the elastic tensor, \mathbf{u} is the displacement, ρ is the density of the material, α is the linear coefficient of thermal expansion, T is the temperature, C_p is the specific heat of the material, K_{bulk} is the bulk thermal conductivity, and Q is the heat source term accounting for the laser heating of the nanograting, as described by Banfi et al. (8). The more complete account of the physical dynamics in our sample allows for a more precise fit to our data and lowers our uncertainty, particular for small-line width samples.

The effective thermal boundary resistivity r_{eff} , which sets the temperature discontinuity, ΔT , across the boundary between the nickel nanostructures and the substrate, is introduced with the following equation:

$$\mathbf{n} \cdot (K_{\text{bulk}} \nabla T) = -\frac{\Delta T}{r_{\text{eff}}}, \quad [\text{S3}]$$

where \mathbf{n} is the unit vector normal to substrate surface.

The simulations provide a time-dependent surface deformation profile, as illustrated in Fig. S3B. Fresnel optical propagation is used to calculate the dynamic diffraction signal from these deformations, which can be directly compared with our experimental observations. For each sample geometry, we calculate the diffraction signals from a comprehensive set of deformation profiles related to different values of r_{eff} . The effective resistivity r_{eff} that then provides the best fit to the experimental data is selected to represent the sum of the constant intrinsic thermal boundary resistivity, r_{TBR} , and corrections due to the nanoscale size effects, r_{Corr} . Insight into the expected size dependence of this correction can be gained from simple models for isolated heat sources from Wexler (9) and Prasher (10). They approximate thermal resistance due to a constriction, R_c , as a sum of a diffusive and ballistic term. In the cylindrical geometry discussed by Siemens et al. (4), these terms are given by the following:

$$R_c = \frac{\ln(P/L)}{K_{\text{bulk}} \pi M} + \frac{4\Lambda_{\text{gray}}}{3K_{\text{bulk}} \pi (L/2)M}, \quad [\text{S4}]$$

where M is the length of the nanowire. To fit our data to a purely diffusive model, we effectively set this sum of terms equal to a single diffusive term with a modified thermal conductivity, K_{nano} , similar to the practice in existing literature:

$$\frac{\ln(P/L)}{K_{\text{bulk}}\pi M} + \frac{4\Lambda_{\text{gray}}}{3K_{\text{bulk}}\pi(L/2)M} = \frac{\ln(P/L)}{K_{\text{nano}}\pi M}. \quad [\text{S5}]$$

$r_{\text{Corr, iso}}$ is then related to the difference in heat flux induced by this modified thermal conductivity at radius d , which encloses the finite region in which nondiffusive effects are important:

$$r_{\text{Corr, iso}} = \frac{d}{K_{\text{nano}}} - \frac{d}{K_{\text{bulk}}} = \frac{4\Lambda_{\text{gray}}d}{3K_{\text{bulk}}(L/2)\ln(P/L)} \propto \frac{\Lambda_{\text{gray}}}{L/2}. \quad [\text{S6}]$$

The size of the region where ballistic effects are important should be determined only by the phonon MFP distribution, so although d can depend on Λ_{gray} of the substrate, it should have no dependence on L or P .

This type of correction was also discussed by Chen (11) and has been widely used in past works (4, 12–16) to account for non-diffusive thermal transport near isolated nanoscale heat sources. The unique insights we present here address how heat transfer is also changed due to the interactions between neighboring nanoscale heat sources and how it is determined by both phonon MFP spectra and heat source arrangements.

All of the material properties used in the finite-element multiphysics modeling are listed in Table S1. Given the maximum substrate temperature change induced in our experiment of ≤ 40 K, the specific heat and bulk thermal conductivity can change by $\leq 10\%$, and we confirm that any change of this magnitude does not cause appreciable differences in the simulated time-dependent diffraction signal we use to compare with experimental data. Moreover, because we observe no pump-fluence dependence in the normalized signals, precise choices for simulation temperatures will not affect the resulting comparison with experimental data.

S3. Model for Interacting Heat Sources

In this work, we introduce a new model to account for the size effects observed in our measurement by using a suppression filter in the phonon MFP spectrum of differential thermal conductivity. The model is derived from the physical limits of diffusive heat transport both for large-line width structures and for the case of uniform heating when period equals line width, as well as the analytically derived resistivity correction for small isolated line heat sources shown above and a particular MFP, Λ :

$$r_{\text{Corr, iso}} \propto \frac{\Lambda}{(L/2)}. \quad [\text{S7}]$$

In addition, we assume that the filter function should be smooth and that the effects of L and P are uncoupled and the same but opposite to each other. The relevant nondimensional variables are L/Λ and P/Λ . All of this behavior is captured by a special case of the generic family of logistic functions:

$$S_L(L/\Lambda) = \tanh\left(\frac{L}{2\Lambda}\right), \quad [\text{S8}]$$

$$S_P(P/\Lambda) = 1 - \tanh\left(\frac{P}{2\Lambda}\right), \quad [\text{S9}]$$

$$S_{\text{total}}(L, P, \Lambda) = S_L + S_P. \quad [\text{S10}]$$

These functions are plotted in Fig. S4A, where we can see the similarity between the shape of S_{total} and standard notch filters. This suppression function can then be applied to each individual

MFP-dependent contribution to thermal conductivity to calculate an effective $K_{\text{nano}} = \sum_i k(\Lambda_i) \cdot S(L, P, \Lambda_i)$.

The resistivity correction for heat transport from interacting nanoscale heat sources can again be related to the change in conductivity imposed by the suppression function:

$$r_{\text{Corr, int}} \propto \frac{1}{K_{\text{nano}}} - \frac{1}{K_{\text{bulk}}}, \quad [\text{S11}]$$

which gives the following:

$$r_{\text{Corr, int}}(L, P) = A \left(\frac{1}{\sum_i k(\Lambda_i) S(L, P, \Lambda_i)} - \frac{1}{\sum_i k(\Lambda_i)} \right). \quad [\text{S12}]$$

The proportionality constant, A , incorporates geometrical constants along with the length scale introduced by the transformation from conductivity to resistivity. We associate this length scale with a finite region within radius d near the heat source in which effective conductivity is modified from the bulk value, and the present model assumes that this length scale is the same for all phonon modes. The correspondence between this model and the previous isolated model (Eq. S4) suggests that A for the 1D line geometry could be written as follows:

$$A = d \ln(P/L). \quad [\text{S13}]$$

Under this assumption, fitting our data with the full multi-MFP interacting model yields values $d_{\text{sapp}} = 123 \pm 10$ nm and $d_{\text{Si}} = 665 \pm 75$ nm. These correspond to one or two times the gray MFP value, which is the region in which one could intuitively expect most nondiffusive effects to be important. We do note that this form for the constant fails in the limit of $P \rightarrow \infty$ for the case of varying duty cycles, because it implies a divergent r_{Corr} regardless of the comparison between L and Λ . However, our data analysis simply fits A as a single scaling constant (with the constant duty cycle describing our data), which does not affect any of the other parameters extracted through the fitting processes. Furthermore, all our simulations and fitting procedures for analyzing our data exist in the effective resistivity picture so that we never need to assume what the length scale, d , might be.

Using the gray model assuming a single MFP (as in the blue curves found in Fig. 2B), the derived $r_{\text{Corr, int}}$ yields a reasonably good approximation for sapphire, but not for silicon. Both are well fit by including the extension to multiple MFPs.

Our model can be used in combination with calculated differential conductivity distributions (like the one shown in Fig. 3A) to test how well they can account for our observations of r_{eff} , including in particular the double-peak structure we observe for the silicon substrate. It can also be inverted to allow the extraction of differential conductivity information from r_{eff} data, as shown in Fig. 4.

The upper and lower bounds of the full range of MFP contributions to which we are sensitive are set by the suppression functions related to each of our nanogratings. We choose the minimum (14-nm) and maximum (5- μm) MFPs of our experimental spectrum to include only MFPs that are suppressed by at least 20% in our smallest and largest sample geometries, respectively. As can be seen in Fig. S4A, each particular configuration for L and P can be related to one most-suppressed MFP—at the minimum of S_{total} . We use this information from our set of nanogratings to set the MFP bins that we use when fitting r_{eff} data in the full interacting multi-MFP model, as shown in Fig. S4B: bin boundaries are chosen halfway between neighboring most-suppressed MFPs.

The weights $k(\Lambda_i)$ fit to each bin give their relative contribution per nanometer to the differential thermal conductivity. The error bars in the histograms of Fig. 4 are obtained by varying $k(\Lambda_i)$ while maintaining the residual of the fit within the range of experimental uncertainty to explore the full range of weights allowed by the shape of the data.

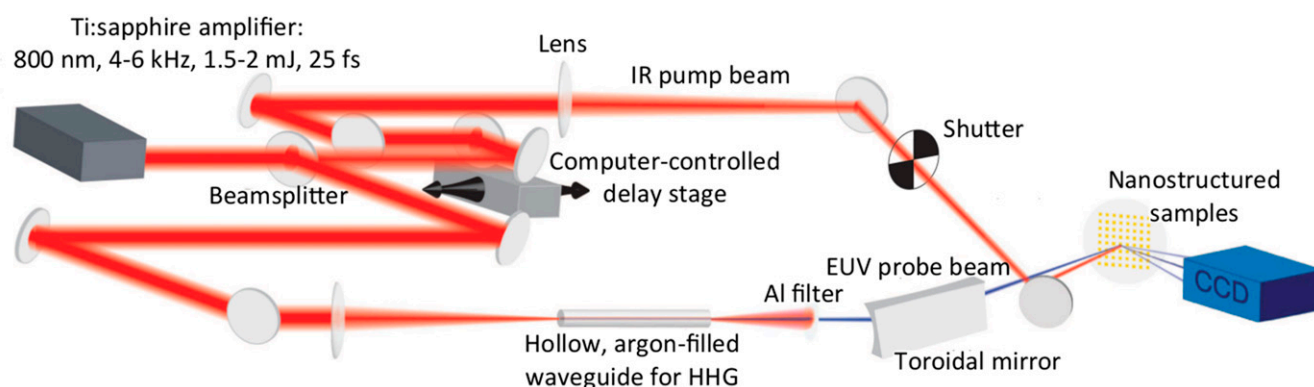


Fig. S1. Experimental setup. Schematic illustration of the pump-probe diffraction measurement, adapted from Siemens et al. (1).

1. Siemens ME, et al. (2010) Quasi-ballistic thermal transport from nanoscale interfaces observed using ultrafast coherent soft X-ray beams. *Nat Mater* 9(1):26–30.

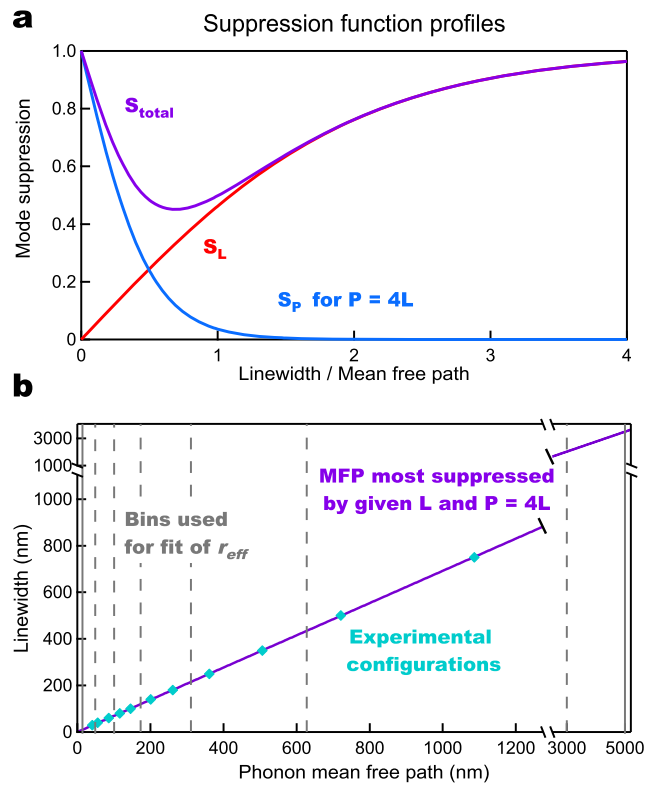


Fig. S4. Visualizing phonon mode suppression. (A) For a phonon mode with a given MFP, S_L describes the suppression of this mode's contribution to thermal conductivity as the line width of a heat source decreases. S_p undoes this suppression, and S_{total} represents the total suppression when both small heat source and interaction between heat sources are taken into account. Thus, each configuration for L and P can be related to one most-suppressed MFP (minimum of S_{total}). (B) We use this information to set the MFP bins used when fitting r_{eff} data in the full interacting multi-MFP model.

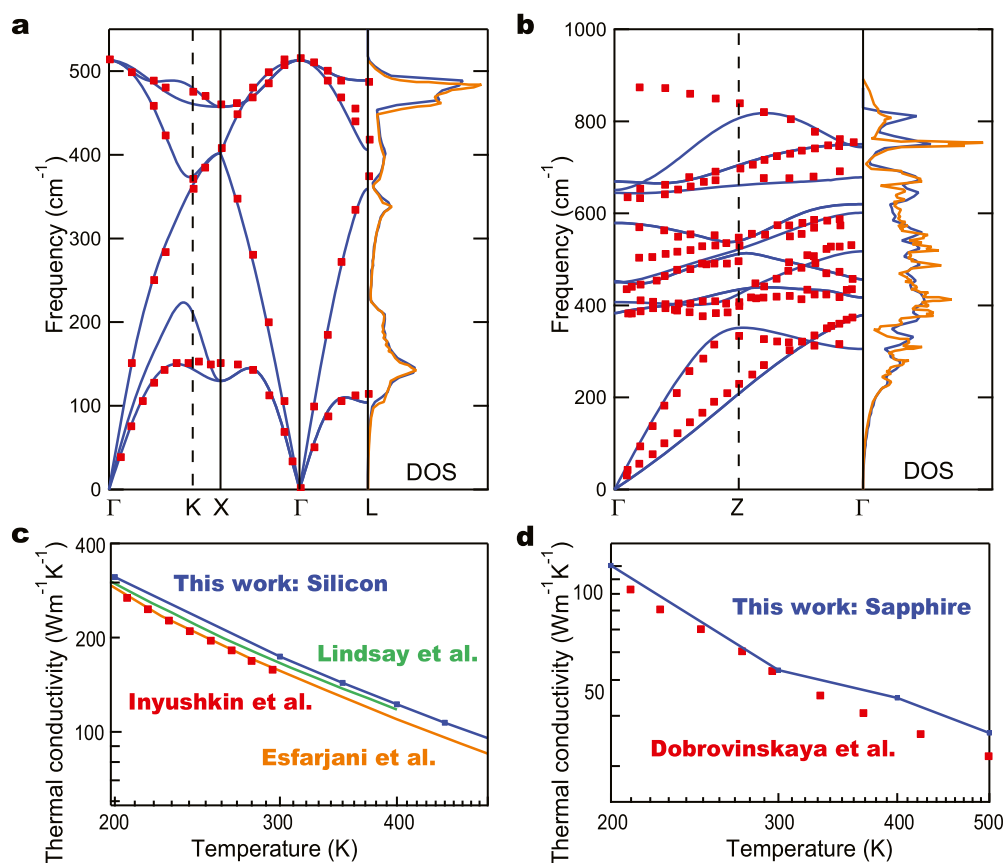


Fig. S5. Comparing our DFT calculations with published work. Calculated phonon dispersion relation and DOS of silicon (A) and sapphire (B) are shown in blue. The red dots in A represent the measured silicon phonon dispersion by Nilsson and Nelin (1), whereas the orange curve is the DOS of silicon calculated by Esfarjani et al. (2) The red dots in B represent the measured sapphire phonon dispersion by Schober et al. (3), and the orange curve is the calculated DOS by Heid et al. (4) Calculated thermal conductivity curves for silicon (C) and sapphire (D) are shown in blue. The red dots in C represent the measured thermal conductivity of isotope-enriched silicon by Inyushkin et al. (5), whereas the orange and green curves are other previous theoretical calculations (2, 6). The red dots in D show the experimentally measured thermal conductivity for sapphire (7).

1. Nilsson G, Nelin G (1972) Study of the homology between silicon and germanium by thermal-neutron spectrometry. *Phys Rev B* 6(10):3777–3786.
2. Esfarjani K, Chen G, Stokes HT (2011) Heat transport in silicon from first-principles calculations. *Phys Rev B* 84(8):085204.
3. Schober H, Strauch D, Dörner B (1993) Lattice dynamics of sapphire (Al_2O_3). *Z Phys B Con Mat* 92(3):273–283.
4. Heid R, Strauch D, Bohnen K-P (2000) *Ab initio* lattice dynamics of sapphire. *Phys Rev B* 61(13):8625–8627.
5. Inyushkin AV, Taldenkov AN, Gibin AM, Gusev AV, Pohl H-J (2004) On the isotope effect in thermal conductivity of silicon. *Phys Status Solidi C* 1(11):2995–2998.
6. Lindsay L, Broido DA, Reinecke TL (2013) *Ab initio* thermal transport in compound semiconductors. *Phys Rev B* 87(16):165201.
7. Dobrovinskaya ER, Lytvynov LA, Pishchik F (2009) *Sapphire: Material, Manufacturing, Applications* (Springer, New York), p 55.

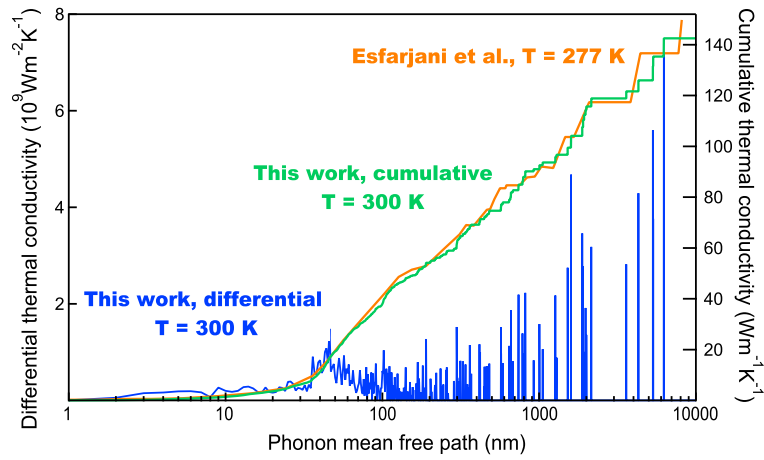


Fig. S6. Thermal conductivity MFP spectra. The differential (blue) and cumulative thermal conductivity (green) of silicon are reported. We also show the cumulative thermal conductivity calculated by Esfarjani et al. (1) (orange).

1. Esfarjani K, Chen G, Stokes HT (2011) Heat transport in silicon from first-principles calculations. *Phys Rev B* 84(8):085204.

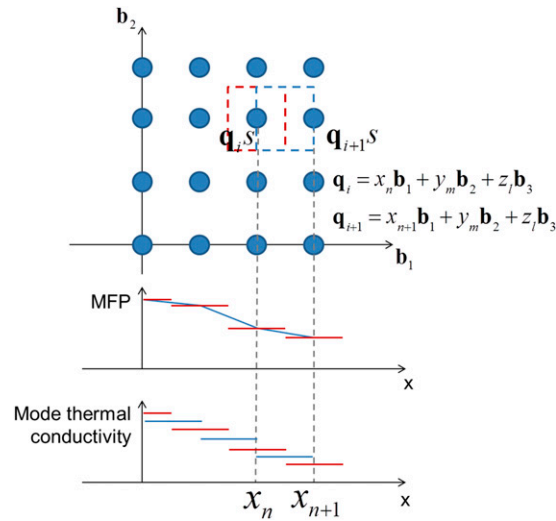


Fig. S7. Schematic of the interpolation process. The first-principles calculations assume that all phonon modes contained within the red box around mesh point \mathbf{q}_s have the same MFP and thermal conductivity as the mode on the mesh point, resulting in discrete spikes in the differential conductivity spectrum. To build the continuous function implied by the discrete spectrum, we interpolate the MFP of phonons in the region represented by the blue box in between the neighboring mesh points and assign to them the average mode thermal conductivity as shown in the bottom two graphs.

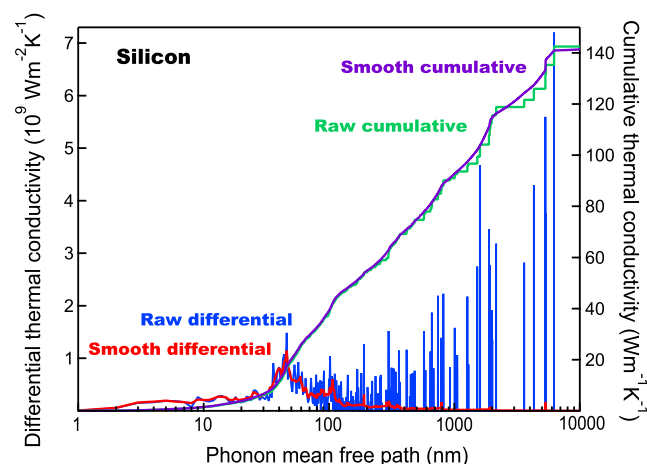


Fig. S8. Interpolating the discrete spectrum. The smoothed differential (red) and cumulative thermal conductivity (purple) compare well with the discrete, raw spectra (blue and green, respectively).

Table S1. Material parameters used in multiphysics simulations

Material properties	Nickel	Silicon	Sapphire
C_p , specific heat (at 300 K), J/(kg·K)	456.8 (1)	710.0 (2)	657.5 (1)
K_{bulk} , bulk thermal conductivity, W/(m·K)	90.9 (2)	149.0 (3)	41.1 (1)
Debye temperature, K (4)	450	645	1047
Poisson's ratio (5)	0.31	0.27	0.25
Young's modulus, 10^{11} Pa	2.00 (6)	1.31 (7)	3.45 (8)
α , linear coefficient of thermal expansion, $10^{-6}/K$	12.77 (1)	3.00 (9)	5.21 (1)
ρ , density, kg/m ³	8,910 (1)	2,330 (10)	4,000 (1)

1. Siemens ME, et al. (2010) Quasi-ballistic thermal transport from nanoscale interfaces observed using ultrafast coherent soft X-ray beams. *Nat Mater* 9(1):26–30.
2. Desai PD (1986) Thermodynamic properties of iron and silicon. *J Phys Chem Ref Data* 15(3):967–983.
3. Dean JA, ed (1999) *Lange's Handbook of Chemistry* (McGraw-Hill, New York), 15th Ed, pp 290–294.
4. Kittel C (1996) *Introduction to Solid State Physics* (Wiley, New York), 7th Ed, pp 126.
5. Nardi D, et al. (2011) Probing thermomechanics at the nanoscale: Impulsively excited pseudosurface acoustic waves in hypersonic phononic crystals. *Nano Lett* 11(10):4126–4133.
6. Zacharias J (1933) The temperature dependence of Young's modulus for nickel. *Phys Rev* 44(2):116–122.
7. Wortman JJ, Evans RA (1965) Young's modulus, shear modulus and Poisson's ratio in silicon and germanium. *J Appl Phys* 36(1):153–156.
8. Wachtman JB, Jr, Tefft WE, Lam DG, Jr, Apstein CS (1961) Exponential temperature dependence of Young's modulus for several oxides. *Phys Rev* 122(6):1754–1759.
9. Okada Y, Tokumaru Y (1984) Precise determination of lattice parameter and thermal expansion coefficient of silicon between 300 and 1500 K. *J Appl Phys* 56(2):314–320.
10. Weber MJ, ed (2003) *Handbook of Optical Materials* (CRC, Boca Raton, FL), p 324.